Ecological Modelling 515 (2026) 111510

Contents lists available at ScienceDirect

Ecological Modelling

journal homepage: www.elsevier.com/locate/ecolmodel

Guerrilla clonal growth strategy leads to amorphous pattern formation in a drylands vegetation model

Andrea Davin [a,*], Jost von Hardenberg [b], Paul M.J. Berghuis [c,d], Ángeles G. Mayor [e], Enrico Magazzino [f,g], Max Rietkerk [d], Frits Veerman [h], Mara Baudena [i,j]

[a] Department of Earth and Environmental Sciences, University of Milan-Bicocca, Milan, Italy
[b] Department of Environment, Land and Infrastructure Engineering, Politecnico di Torino, Turin, Italy
[c] Department of Coastal Systems, Royal Netherlands Institute for Sea Research, Den Burg, The Netherlands
[d] Copernicus Institute of Sustainable Development, Environmental Sciences, Utrecht University, Utrecht, The Netherlands
[e] Department of Ecology, University of Alicante, Alicante, Spain
[f] Department of Land, Environment, Agriculture and Forestry (TESAF), University of Padova, Legnaro, Italy
[g] Interdepartmental Research Center of Geomatics (CIRGEO), University of Padova, Legnaro, Italy
[h] Mathematical Institute, University of Leiden, Leiden, The Netherlands
[i] Institute for Atmospheric Sciences and Climate (ISAC), National Research Council (CNR), Turin, Italy
[j] National Biodiversity Future Center (NBFC), Palermo, Italy

ARTICLE INFO

Dataset link: https://github.com/A-Davin/clonal_guerrilla

Keywords:
Drylands
Vegetation
Patterns
Clonality
Numerical modelling
Non-linearity
Self-organization

ABSTRACT

Resource concentration in the vicinity of plants is observed in drylands as a result of various mechanisms, developed to cope with water scarcity. This often leads to self-organized spatial patterns that enhance drylands' ecosystem resilience to environmental changes. Numerous vegetation dynamics models have been developed over the past few decades to study this pattern formation. Generally, they represent plant spatial spread as a diffusive process, which captures well species that reproduce via seed dispersal or through clonal growth following the "phalanx" strategy, characterized by slow, compact expansion. However, many dryland species exhibit "guerrilla" clonal growth, characterized by rapid, directional exploration of favourable areas, which is poorly captured by diffusion. To address this limitation, we introduce a novel term for lateral biomass expansion into a classical dryland model.

We found conditions suitable for periodic patterns to emerge with a Turing analysis, aiming to test the stability of a uniform solution against uniform and periodic perturbations. However, numerically, these patterns could not be observed by perturbing the homogeneous equilibria with small perturbations, possibly because of the non-linearity of the guerrilla expansion term. Instead, remarkably, the model produced amorphous, far-from-equilibrium patterns when integrated along a rainfall precipitation gradient.

These findings highlight the need to represent the diversity of clonal plant strategies in dryland ecosystem models, as they play an important role in pattern formation and, thus, may influence ecosystem resilience and responses to global environmental change. Furthermore, our results highlight the need to move beyond linear analyses when studying systems with nonlinear dispersal dynamics.

1. Introduction

Drylands are ecosystems characterized by water scarcity that constitute 46% (Abatzoglou et al., 2018) of the Earth's land area (Food and Agriculture Organization of the United Nations (FAO), 2019). In drylands, water scarcity triggers competition among vegetation for water and adaptations that allow plants to either ameliorate their own environment, for example, by increasing soil infiltration, or to optimize their water uptake and use (e.g., by shedding their leaves during drought or by having deep root systems).

A distinctive feature of drylands is the presence of regular (i.e., periodic, Turing) patterns (such as spots, stripes, labyrinths, and gaps) (Deblauwe et al., 2008) or irregular patterns (i.e., non-periodic, scale-free) (Borgogno et al., 2009) observed worldwide. Pattern formation seemingly contributes to the resilience of plant communities to environmental changes, such as rising temperatures or reduced rainfall (Rietkerk et al., 2021; Kéfi et al., 2024), thus highlighting the relevance of this process. The presence of patterns has been connected to the existence of a 'scale-dependent feedback', i.e., feedback between plants and soil

* Corresponding author.
E-mail address: a.davin@campus.unimib.it (A. Davin).

https://doi.org/10.1016/j.ecolmodel.2026.111510
Received 8 August 2025; Received in revised form 13 January 2026; Accepted 25 January 2026
Available online 2 February 2026

water that is positive near the plant but becomes negative further away (Rietkerk et al., 2002). Given that the amount of available water is not sufficient to allow continuous plant cover, some plant adaptations to water scarcity lead to increased resources locally, for example by ameliorating soil and increasing water infiltration within plant patches with respect to bare soil (Rietkerk et al., 2002), or by larger plants having a wider extension of the underground root system, allowing them to reach water further away (i.e., the root-augmentation feedback (Gilad et al., 2004)). These mechanisms lead to a positive feedback near a plant patch. The feedback, however, becomes negative at larger distance from a plant, where water competition with neighbouring plants prevails. As a result, the growth of new plants is favoured in the vicinity of existing plant patches and reduced elsewhere, leading to the formation of vegetation patterns, as shown by numerous mathematical models primarily employing partial differential equations (Gilad et al., 2004; Bastiaansen et al., 2018; Siero et al., 2019; Bennett et al., 2022).

Clonal growth, which enables plants to extend without relying on sexual reproduction, is quite common in drylands. For example, they have been observed in up to 65% of the total plant species in Australian shrub-dominated drylands (Tsakalos et al., 2022). A clonal colony, or "genet", is a group of individuals, each one genetically identical and interconnected to the others. In plants, an individual from such population is referred to as a "ramet". Each ramet has its own life cycle. Clonal plants' growth in space proceeds by extending the apices of the ramets or growing new branches above and beyond those of already established plants, even within the same community. Therefore, the direction in which new shoots grow plays an important role during genet's development (Oborny et al., 2012). Based on possible differences in shoot length and branching angles, two main strategies are defined: "phalanx" and "guerrilla" (Oborny et al., 2012). In the phalanx strategy, new ramets grow close to the older ones, with relatively short internode lengths and spreading in a wide range of branching angles (Fig. 1b). This pattern results in a dense, spatially aggregated expansion (Fig. 1d.) The guerrilla strategy, by contrast, involves the production of more sparsely spaced ramets, with narrower branching angles than those observed in the phalanx strategy, and internodes length described as following heavy-tailed step-length distributions (Reijers et al., 2021). This implies that short-distance steps are interspersed by rare long-distance steps (Fig. 1a). Plants that adopt this approach reduce self-competition among ramets originating from the same mother organism allowing for rapid exploration of the surrounding environment (Fig. 1c). Notably, these two strategies reflect the extremes of what is, in fact, a spectrum rather than a rigid classification (Sintes et al., 2006; Chen et al., 2011). Although species that follow one of these "extreme" strategies exist, clonal plants generally shift along the continuum during their life cycle or in response to changing external conditions (Oborny et al., 2012; Oborny, 2019).

Previous modelling works have explored the architecture of clonal plants using a variety of approaches, each addressing distinct biological questions. For instance, Oborny et al. (2001) employed a spatially explicit, module-based framework to show that clonal growth strategies can shift plastically in response to spatially heterogeneous resource availability. That transport between ramets regulates the balance between exploration and exploitation in patchy environments. Instead, Herben and Wildová (2012) investigated a similar individual-based approach, how species-specific architectural traits shape coexistence and performance among multiple clonal species at the community scale.

Understanding clonal growth dynamics is particularly relevant in drylands, as plants favour clonal propagation over sexual reproduction in response to environmental stress (Yu et al., 2008; Luo et al., 2018; Ma et al., 2019), allowing the genet to share nutrients and water among its ramets and, thus, making those placed in stressed areas more resilient (Oborny, 2019; Liu et al., 2016). Most of the numerical models of dryland vegetation pattern formation typically represent the spatial expansion of plants as a diffusion process (von Hardenberg et al., 2001; Gilad et al., 2004; Bastiaansen et al., 2018). This approach is a reasonable approximation for representing plant lateral growth, local seed dispersal (i.e., short-range, thus excluding transport by wind and/or animals over long distances) and the phalanx strategy in clonal growth, as these processes can be approximated as a Brownian motion. To extend this framework, other models, namely (Pueyo et al., 2010; Baudena and Rietkerk, 2013), incorporated more complex, non-local integral terms to account for long-range vegetation expansion through seed dispersal. However, these models do not include specific terms for guerrilla clonal growth, as diffusion does not represent that strategy equally well. In fact, the guerrilla strategy is characterized by irregular spatial expansion, with variable step lengths (even though there is usually a preferred distance for the offsprings) and the branching angles between new ramets and the branch that generated them are constrained (Oborny et al., 2012).

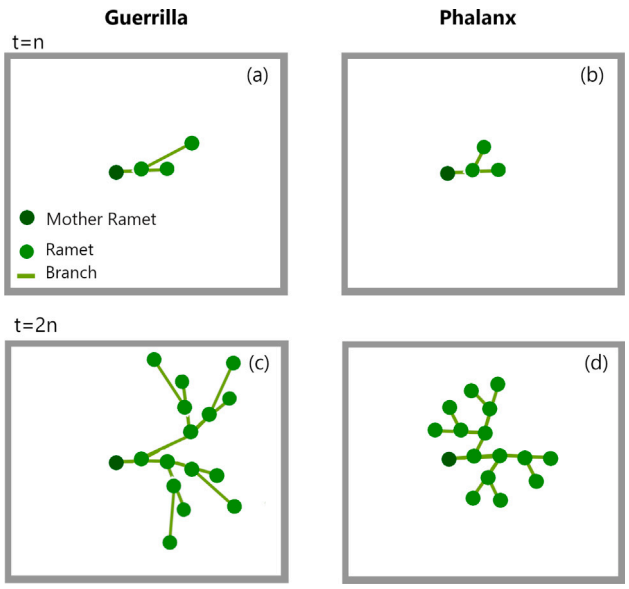

Fig. 1. Schematic representation of the guerrilla and phalanx strategies. (a) The guerrilla genet displays ramets with narrow branching angles and broad step length distribution, while (b) the phalanx predicts broader branching angles and a narrow step length distribution. (c, d) The evolution of the two genets obtained by repeating the previous structure.

Some models have already attempted to reproduce clonal growth including guerrilla strategy in biomes other than drylands. Sintes et al. (2006) developed an agent-based model to reproduce the growth of a single genet by setting growth rules depending on variables such as the sprouting distance, the branching rate or the branching angle. This model successfully captured the transition from guerrilla to phalanx growth, in which the initial expansion follows an irregular, exploratory pattern that is later abandoned in favour of the phalanx strategy. More recently, Bennett et al. (2022) proposed a Partial Differential Equation (PDE) model to represent the invasion of a pantropical clonal shrub *Guilandina bonduc* L., in the tropical island of Trinidad, at the expense of the endemic sedge *Cyperus atlanticus*. Their model included an integral term with a heavy-tailed kernel, conceptually similar to the root-augmentation feedback term present in von Hardenberg et al. (2001) and Gilad et al. (2007). The latter term acts on a long-range, allowing for non-local clonal expansion, as found in in-situ observations (Bennett et al., 2022).

The success of these models in representing simplified clonal plant communities motivates us to employ a similar PDE approach to fill the gap in modelling the guerrilla strategy for dryland plants and to relate it to the key processes of pattern formation that influence dryland resilience and resistance to perturbation and degradation. We present

a new PDE model that captures the whole range of clonal growth strategies. This model explicitly incorporates a term to represent the guerrilla clonal growth strategy. Our guerrilla expansion term builds on recent efforts to conceptualize movement and spatial expansion in clonal plants as Lévy walks (Reijers et al., 2021). While a PDE framework cannot explicitly reproduce such processes, the guerrilla term captures their community-level features. Our aim was to investigate whether or not the inclusion of the guerrilla clonal strategy led to self-organization into spatial patterns. To achieve this, we conduct a bifurcation analysis of the non-spatial model, a Turing analysis of the spatial model, and numerical analyses along a precipitation gradient. We show that the nonlinearity introduced by the new guerrilla clonal growth term can shift solutions from Turing patterns (similarly to what observed in previous models (von Hardenberg et al., 2001; Gilad et al., 2007)) towards far-from-equilibrium solutions (Veerman et al., 2021), depending on the prevailing clonal growth strategy the plants adopt.

2. Methods

2.1. The clonal growth model

The "clonal growth model" proposed in this work is derived from Gilad et al. (2004), which was originally developed to reproduce the growth and spatial organization of vegetation in drylands. The clonal growth model is derived from a simplification of Gilad's model, with the addition of a new term specifically conceived to represent guerrilla growth strategy. With the present model, we thus have two distinct spatial terms representing both clonal strategies, which enables the model to reproduce the whole spectrum of clonal growth strategies.

The clonal growth model is composed of two PDEs for the dynamics of the aboveground biomass density b and the soil moisture w. To focus on the effects of the newly introduced term for the guerrilla growth strategy, Gilad's model was simplified from three to two PDEs by making two main assumptions. First, we assumed that precipitation infiltrates immediately into the ground; thus, we could remove the equation for overland flow and the term representing the infiltration feedback. Secondly, we neglected the effect of shading in limiting soil evaporation. The system simulates idealized conditions, namely constant precipitation, flat topography and absence of spatial or temporal disturbances or heterogeneities.

The system in its non-dimensional (i.e., unitless) form is:

$$\frac{\partial b}{\partial t} = g_b(1-b)b - b + \nabla\cdot\mathbf{f} + \delta_b\nabla^2 b, \tag{1a}$$

$$\frac{\partial w}{\partial t} = p - \nu w - g_w w + \delta_w\nabla^2 w \tag{1b}$$

in which

$$g_b = \nu\int_\Omega g(\mathbf{x},\mathbf{x}',t)w(\mathbf{x}',t)d\mathbf{x}', \tag{2a}$$

$$g_w = \gamma\int_\Omega g(\mathbf{x}',\mathbf{x},t)b(\mathbf{x}',t)d\mathbf{x}', \tag{2b}$$

$$g(\mathbf{x},\mathbf{x}',t) = \frac{1}{2\pi}\exp\left[-\frac{|\mathbf{x}-\mathbf{x}'|^2}{2(1+\eta b(\mathbf{x},t))^2}\right] \tag{2c}$$

In which $\mathbf{x} = \begin{pmatrix} x \\ y \end{pmatrix}$.

An extended description of how non-dimensional equations can be obtained by scaling is reported in Gilad et al. (2007). The parameter values (see Table 1) were, except for the much smaller diffusion coefficient (for the reasons explained above), taken from Gilad et al. (2007), as this study represented shrubs, which often display clonal reproduction (Jenik, 1994).

The (normalized) biomass density b can range between 0 and 1. Its equation (Eq. (1a)) is based on a logistic equation modulated by a kernel term g_b (Gilad et al., 2004). The latter represents how growth depends on water availability both at the plant location and in the neighbourhood of its roots, and it is computed over the entire domain Ω, which is assumed to be infinite relative to the scale of the minimal length unit x. The positive feedback between the biomass of a plant and its root extension is included in the dependence of the root length on biomass: the larger the biomass, the smaller the decay with distance of the function g, and thus the longer the roots' range for water uptake.

Table 1
Non-dimensional parameter symbol, name and values.

Parameter	Bio-Physical meaning	Value
ν	Soil water evaporation rate	3.33
η	Root augmentation	3.50
γ	Soil water consumption rate	16.66
c	Clonal reproduction velocity	0.20
δ_b	Biomass growth regularization	0.0005
δ_w	Transport coefficient for soil water	3.33
p	precipitation rate	0–8

The other terms in the equation are, respectively, a mortality term $-b$, the novel "clonal expansion term" $\nabla\cdot\mathbf{f}$ (whose form will be discussed in the next section) and finally the diffusion term $\delta_b\nabla^2 b$. This latter term allows for the inclusion of the phalanx clonal strategy. As our aim for this study was to investigate the effects of this new term and of the guerrilla strategy, we set δ_b to a very small value. However, we did not set $\delta_b = 0$ for mathematical reasons, namely to avoid the insurgence of vegetation patterns below a physically meaningful scale (see Section 3.1.2 for a mathematical explanation and Appendix B for a graphical one). The water dynamics (Eq. (1b)) depends on the precipitation input, p, which is a positive quantity that in this study we consider in the range between 0 and 8, representing a wide range of precipitation rates that spans from arid regions to the higher limit of dry sub-humid ones (i.e., up to about 1200 mm year) (Food and Agriculture Organization of the United Nations (FAO), 2004). Soil water outputs are evaporation νw and root uptake $g_w w$. The last term on the right hand side represents moisture diffusion in the soil $\delta_w\nabla^2 w$. As biomass growth is interdependent with plant transpiration, the water uptake term also includes an integral over the domain Ω, to represent how water at a certain location can be withdrawn by the roots of the plants in the neighbourhood, and thus includes the same kernel term g representing root spread, but with a "switched" dependency on x (the local position) and x' (the neighbourhood) (Gilad et al., 2004). Thus, the dynamics of biomass b and soil water w are coupled through the integral terms.

2.2. Guerrilla expansion term

We defined the novel guerilla clonal term as a flux of a driving quantity $\mathbf{f}$, i.e., there is a local function $\mathbf{f}$ that influences the expansion rate of vegetation. In earlier models, including only diffusion, this driving quantity was the biomass gradient, i.e., the difference in biomass quantity among neighbouring points (von Hardenberg et al., 2001; Gilad et al., 2004).

Here, we define the term as:

$$\nabla\cdot\mathbf{f} = c\nabla\cdot(bw\frac{\nabla b}{|\nabla b|}) \tag{3}$$

The term's form derives from the following considerations:

- It is assumed that multiple individual plants grow in a relatively small space; thus, biomass will grow in every direction. Therefore, despite the guerrilla clonal expansion of an individual plant being asymmetrical, we introduced a symmetrical term to represent patch expansion.
- The biomass density gradient is normalized to determine the direction of growth. Thus, a spot expands radially towards areas with lower biomass density (as in a diffusion term). Still, the expansion rate is independent of the magnitude of the biomass density gradient. This is meant to reproduce the observation that

clonally guerrilla-growing plants will extend their stolons in any direction, independently of neighbouring plants (Winkler et al., 1999).

In numerical integration, we added an $\epsilon = 10^{-20}$ to the biomass density gradient norm in the denominator to avoid issues whenever $\nabla b = 0$. Including this term did not affect the mathematical analyses reported below.

- Areas characterized by high density will colonize neighbouring areas faster than those with a sparser vegetation: this consideration is represented by $\mathbf{f}$ being linear in b.
- The dependence of $\mathbf{f}$ on w is justified by the observation that ramet establishment depends on water availability (Pessarakli, 2017). It also includes the assumption that the plasticity of the genets depends on water availability. The latter consideration implies that the vegetation explores more rapidly regions around areas that can sustain more biomass because of their higher soil water content.
- The factor c defines the velocity of the expansion, which we considered constant.

  Thus, this term allows biomass to extend in the direction of its own gradient, but more rapidly where the local bw product is stronger. In other words, ∇b determines the direction of growth while the rate at which plants expand depends on the local availability of both water and biomass. Without including the water w instead, this term would be more similar to the commonly used diffusion term, in which plants only grow towards areas with lower biomass density.

2.3. Analyses

2.3.1. Linear stability analysis

We started from the linear stability analysis of the uniform states. To find those solutions, the stationary equations, obtained by setting both time- and space-dependent derivatives of the system to zero, were solved using a symbolic calculation software (Mathematica v. 13.1). To study the stability of the solutions to homogeneous perturbations, the variables were perturbed by a term that depends only on time: $\delta b(t) = a_b \exp(\lambda t)$, $\delta w(t) = a_w \exp(\lambda t)$ and a linear stability analysis was performed.

The analytical study of the linear stability also required solving the integral terms present in the clonal growth model. These were solved as reported in Appendix A by integrating over the domain Ω.

2.3.2. Turing stability analysis

Turing stability analysis was performed similarly to what just described, but considering spatially-dependent perturbations of the two variables characterized by a constant wavelength k: $\delta b(x,t) = b' \exp(ik \cdot x + \lambda t)$ and $\delta w(x,t) = w' \exp(ik \cdot x + \lambda t)$.

By plotting the real part of the eigenvalues relative to the uniformly vegetated state against an interval of k, we could describe which is the fastest-growing perturbation. After determining that wavelength, we used it to plot the real part of the eigenvalues relative to the two states as a function of precipitation rate to identify the precipitation range in which the system is sensitive to Turing pattern formation.

2.3.3. Numerical simulations

First, we perturbed the stable solutions with a periodic perturbation characterized by a small amplitude ($\sim 5\% b$ of the equilibrium solution) to follow up on the mathematical analysis. Surprisingly, as will be illustrated in Section 3.2, these perturbations were quickly dampened and the system returned to the uniform condition. To further test the divergence between the mathematical analysis and the numerical results, we then used similar sinusoidal perturbations but with a larger amplitude than before ($\sim$ 20%b of the equilibrium solution). The comparison is discussed in Appendix D. Throughout the rest of the paper, to verify whether pattern formation could occur nonetheless, we used what we name "realistic initial conditions", i.e., conditions in which biomass density was initialized to $b = 0$ everywhere with the exception of randomly selected gridpoints, representing $\sim 1\%$ of the total, where biomass density was set to $b = 0.4$. Soil water content was uniform across the entire spatial domain. This initialization, derived from Rietkerk et al. (2002), was meant to reproduce conditions similar to a dryland, where plant patches are interspersed within bare soil (Deblauwe et al., 2008; Borgogno et al., 2009).

To analyse the effects of the new term representing guerrilla clonal growth on pattern formation, we also compared runs obtained with two different parameter settings to represent plants with either predominantly phalanx ($c = 0.05, \delta_b = 0.333$) or guerrilla growth strategies ($c = 0.20, \delta_b = 0.0005$). Results from the comparison of the two runs are introduced in Section 3.2 and further discussed in Appendix E. Furthermore, we run simulations with the standard parameter setting along a gradient of precipitation p spanning from $p = 0$ to $p = 8$.

In the code (written in Julia language), we employed Adams–Bashforth as a solver in time, i.e., a linear multi-step method with an adaptive time-step. The grid employed for the runs consisted of a square of 512 × 512 points, representing a domain size of 28 × 28 non-dimensional units of length.

The equations were integrated over 100 non-dimensional time units (corresponding to about 80 years), unless otherwise specified, for a few runs in which we wanted to test the pattern temporal development. This choice was primarily motivated by the long computational times required to perform the integration, but also by the fact that, detailed in Section 3.2, after $\simeq 70$ time units the patterns evolve more and more slowly in comparison with earlier time steps.

3. Results

3.1. Stability analysis of the homogeneous solutions

Three homogeneous solutions were found: the first represents a bare-soil state, characterized by $b_0 = 0$ and $w_0 = \rho/\nu$, while the other two solutions, found for $p > \sim 0.992$ represent a uniformly vegetated state, whose values of biomass density are, respectively, an increasing and decreasing functions of p (the whole expression is reported in Appendix F). The biomass density value of the third solution keeps decreasing below zero, rendering it a non-physical solution.

3.1.1. Uniform perturbations

To perform the linear stability analysis against uniform perturbations, the integral solutions for a homogeneous domain were substituted in the equations:

$$\begin{cases} \frac{\partial \delta b}{\partial t} = & \nu[\sigma^2(w_0+\delta w) - b_0 - \delta b \\ & + 2\eta\sigma\delta b(w_0+\delta w)](b_0+\delta b)(1-b_0-\delta b) \\ \frac{\partial \delta w}{\partial t} = & p - \nu(w_0+\delta w) \\ & - \gamma[\sigma^2(b_0+\delta b) + 2\eta\sigma\delta b(b_0+\delta b)](w_0+\delta w) \end{cases} \quad (4)$$

where $\sigma = (1 - \eta b)$. Zero-order terms satisfy the stationary conditions, therefore, they can be cancelled out. The system can be further simplified by not considering second-order terms.

The linear stability of the two homogeneous solutions was tested against uniform perturbations (Fig. 2). Expressing the latter as $\delta a = \begin{pmatrix} \delta b \\ \delta w \end{pmatrix} = \begin{pmatrix} a_b \\ a_w \end{pmatrix} e^{\lambda t}$, it was possible to solve the system as an eigenvalue problem:

$$\lambda \begin{pmatrix} a_b \\ a_w \end{pmatrix} = J \begin{pmatrix} a_b \\ a_w \end{pmatrix}$$

where J is the Jacobian.

After the substitution of the two homogeneous solutions, the eigenvalues were calculated as a function of the precipitation rate, in order to derive the stability of their relative states: if both eigenvalues are

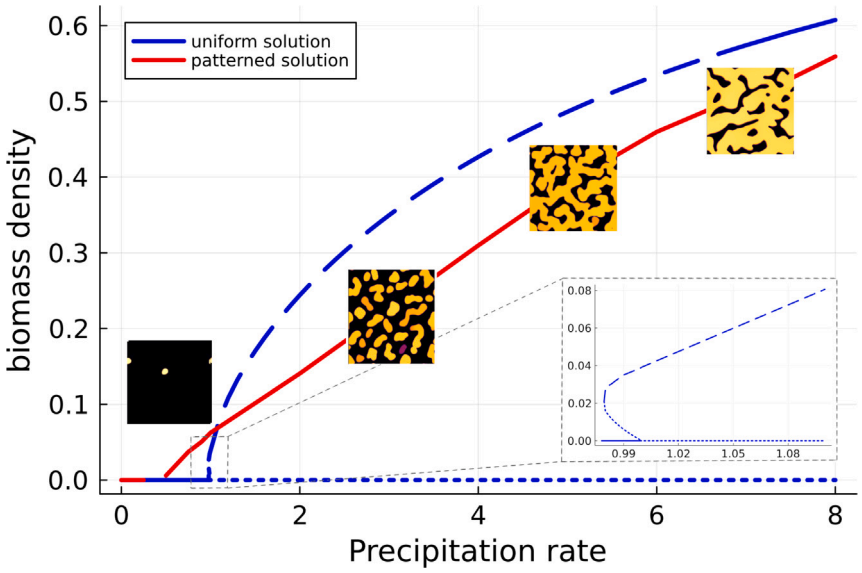

Fig. 2. Bifurcation plot of biomass density b as a function of precipitation p. Blue lines represent the uniform solutions, the red line is the average biomass density for patterned states (after 100 time units). Both quantities are non-dimensional. Solid lines denote linearly stable states to uniform perturbations, dotted lines linearly unstable states, and dashed lines solutions unstable to periodic perturbations. Inset: enlargement of the area indicated with a small square, displaying the bistable range of uniform states when space is not considered.

negative, then the state is stable for that precipitation rate; in the other cases, it is unstable.

Starting from the bare soil state, the system is reduced to the following equations:

$$\begin{cases} \frac{\partial \delta b}{\partial t} = & \nu\sigma^2[\delta w b_0(1-b_0) + \delta w_0(1-b_0)] \\ & + 2\nu\eta\sigma\delta b w_0 b_0(1-b_0) - \delta b \\ \frac{\partial \delta w}{\partial t} = & -\nu\delta w - \gamma[\sigma^2(w_0\delta b + b_0\delta w) + 2\eta\sigma w_0 b_0 \delta b] \end{cases} \tag{5}$$

The corresponding Jacobian is therefore:

$$\begin{pmatrix} \nu\sigma^2(1-2b_0)w_0 + 2\nu\eta\sigma w_0 b_0(1-b_0) - 1 & \nu\sigma^2 b_0(1-b_0) \\ -\gamma w_0\sigma[\sigma + 2\eta b_0] & -\nu - \gamma\sigma^2 b_0 \end{pmatrix} \tag{6}$$

The latter problem can be solved by substituting the variable values into the Jacobian, thereby yielding two eigenvalue problems. The first, relative to the bare-soil state, is solved as shown:

$$\lambda \begin{pmatrix} a_b \\ a_w \end{pmatrix} = \begin{pmatrix} p-1 & 0 \\ -\frac{\gamma p}{\nu} & -\nu \end{pmatrix}$$

The eigenvalues relative to this problem are:

$$\lambda_{(+,-)} = \frac{1}{2}(p - \nu - 1 \pm p + \nu - 1)$$

so $\lambda_{(-)} = -\nu < 0$ and $\lambda_{(+)} = p - 1$.

The second eigenvalue becomes positive for $p > 1$, above which, thus, the bare soil state becomes unstable with respect to spatially homogeneous perturbations. The uniformly vegetated solutions were studied similarly, resulting in the first state being stable for $p > 0.992$, while the second being unstable in the range $0.992 < p < 1$ (inset in Fig. 2). At $p = 1$, there is a transcritical bifurcation, where the second non-trivial steady state exchanges stability with the bare-soil steady state.

The clonal growth model displays also a narrow bistability range (Fig. 2).

3.1.2. Periodic perturbations

The stability of the uniform solutions was evaluated against periodic perturbations of the form $\delta a(x,t) = \begin{pmatrix} \delta b(x,t) \\ \delta w(x,t) \end{pmatrix} = \begin{pmatrix} a_b \\ a_w \end{pmatrix} \exp(ik \cdot x + \lambda t)$, were k is the wavenumber of the perturbation. Here, we included all spatially dependent terms in the systems, i.e., the diffusion terms and the guerrilla expansion term. The latter was included by considering its expansion (see Appendix B for the calculations), obtaining:

$$\nabla \cdot (bw\frac{\nabla b}{|\nabla b|}) = w|\nabla b| + \frac{bw}{|\nabla b|}\nabla^2 b + \nabla w \cdot \frac{b\nabla b}{|\nabla b|} - \frac{bw}{|\nabla b|^3}((\partial_x b)^2\partial_{xx} b + (\partial_y b)^2\partial_{yy} b + 2\partial_x b\partial_y b\partial_{xy} b)$$

Restricting to first-order terms only, the guerrilla expansion becomes (see Appendix A.3 for the whole calculation):

$$\nabla \cdot (bw\frac{\nabla b}{|\nabla b|}) \simeq ik(w_0\delta b(x,t) + b_0\delta w(x,t))$$

Regarding the integral terms, when the perturbation has an explicit, spatially-periodic component, their solution is given by (calculations reported in Appendix A):

$$g_b = \nu[w_0\sigma^2 + 2\eta\sigma w_0\delta b(x,t) + \sigma^2\exp(-\frac{k^2\sigma^2}{2})\delta w(x,t)]$$

$$g_w = \gamma[b_0\sigma^2 + \sigma\exp(-\frac{k^2\sigma^2}{2})\delta b(x,t)(1 + \eta b_0(2 - \sigma^2 k^2))]$$

The corresponding eigenvalue problem, obtained by substituting these solutions in the system, is therefore:

$$\lambda \begin{pmatrix} \delta b \\ \delta w \end{pmatrix} = \Lambda(k) \begin{pmatrix} \delta b \\ \delta w \end{pmatrix} \tag{7}$$

where $\Lambda(k)$ is the Jacobian matrix whose elements are:

$$\Lambda(k)_{11} = \sigma\nu w_0[1 - 2b_0 + \eta b_0(3 - 4b_0)] - 1 + ickw_0 - \delta_b k^2 \tag{8}$$

$$\Lambda(k)_{12} = \nu b_0(1-b_0)\sigma^2\exp(-\frac{k^2\sigma^2}{2}) + ickb_0 \tag{9}$$

$$\Lambda(k)_{21} = -\gamma\sigma w_0\exp(-\frac{k^2\sigma^2}{2}) \cdot (1 + \eta b_0(2 - \sigma^2 k^2)) \tag{10}$$

$$\Lambda(k)_{22} = -\nu - \gamma b_0\sigma^2 - \delta_w k^2 \tag{11}$$

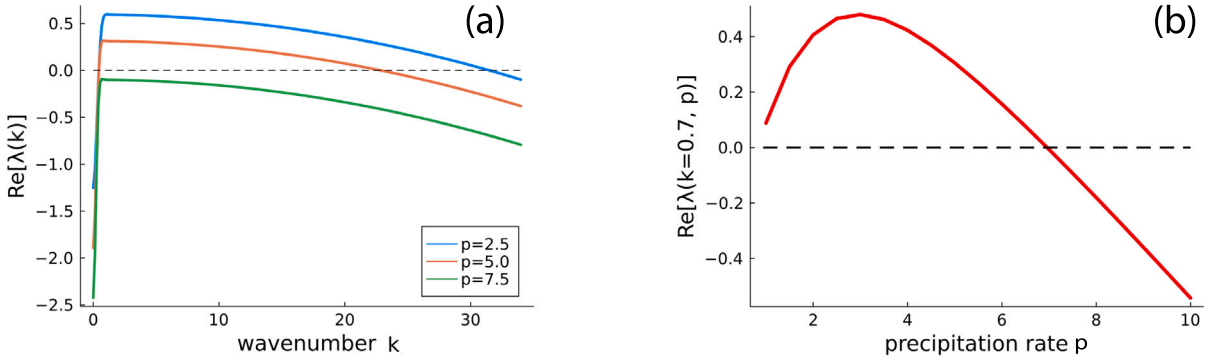

Fig. 3. Results of the Turing analysis: the real part of the largest eigenvalue of the non-trivial, homogeneously vegetated state, plotted as a function of the wavenumber of the perturbation k (a) and the precipitation rate p (b). The ranges of the independent variables in which these functions are positive define the conditions for the formation of Turing patterns. In (a) at values of p far from $p_c \simeq 7.1$ there is a broad range of growing perturbations. Increasing the precipitation rate shifts the graph downward, reducing the range of growing wavelengths. In (b) the second eigenvalue is not represented since it is always negative and with an order of magnitude of 10^3; the eigenvalues were evaluated for $k = k_{max}$.

The Turing stability analysis (Fig. 3(b)) predicts that for precipitation rates $p > p_c \simeq 7$, no perturbation of the homogeneous solution can grow. Close to p_c, the eigenvalue curve assumes a parabolic shape, increasing steeply to a peak around $k_{max} \simeq 0.6$, similarly to what shown with the model of Gilad et al. (2007). However, for lower precipitation rates, the eigenvalue curve decreases slowly with wavenumbers larger than k_{max} (Fig. 3(a)), making the peak less defined, and the homogeneously vegetated state is unstable for a broad range of periodic perturbations. The latter range widens with decreasing p, reaching $k = 32$ for $p = 2.5$, as seen in Fig. 3(a).

When the diffusion term is not included ($\delta_b \nabla b^2 = 0$), the Turing analysis shows that for $p <\sim 7$, all modes above k_{max} can grow. This is due to the absence of the term $-\delta_b k^2$ from the eigenvalue equation (see Eq. (6)), which is what regulates the decrease of the eigenvalue curve with increasing k after the peak around k_{max}. Not having such a limit would mean that any infinitesimally small change in biomass distribution would be able to grow indefinitely. See Appendix B for more details. For this reason, in this paper we set a small positive δ_b (as per Table 1), so that the model avoids this artifact without exceeding in magnitude the growth rate imposed by the clonal expansion term. As mentioned before, diffusion remains an ecologically supported way to represent plant expansion; therefore, it is reasonable to retain the diffusion term, while at the same time using a very small diffusion constant allows us to focus more clearly on the effects of the newly introduced guerrilla expansion term.

As the precipitation rate increases, the range of unstable modes shrinks (Fig. 3a, until, beyond a critical value $p_c \simeq 7.1$, the homogeneous state becomes stable to any periodic perturbation (Fig. 3(b)).

3.2. Numerical simulations

Numerical integrations with periodic initial conditions resulted in the dampening of the periodic perturbation when its amplitude was set to $\sim 5\% b$ of the equilibrium solution, with the system quickly returning to the uniform solution. The periodic perturbation was amplified by the system only when its initial amplitude was large (see Appendix D for an initial perturbation with amplitude set to $\sim 20\% b$ of the equilibrium solution).

Noticeably, numerical integrations starting from the realistic initial conditions, with $c = 0.2$, resulted in the formation of spatially "amorphous" patterns (Fig. 4). Here we define amorphous as irregular patterns that are not scale-free: the patterns we retrieved were characterized by various patch sizes and non-geometrical shapes, but their patch size distribution (Fig. E.11, in Appendix E) did not follow a power law (Kéfi et al., 2007). We then could show that these amorphous patterns were related to the new term representing guerrilla clonal growth, since the model reproduces regular patterns when the parameter values reflect vegetation that mainly adopts the phalanx strategy. On the contrary, as the guerrilla growth term becomes more predominant, the solution shifted towards amorphous patterns (see graphical abstract and Appendix E for more details regarding patch size distribution and characteristic length scales, and the comparison of the two strategies).

Runs performed using the standard parameter values (i.e., those reported in Table 1), with increasing precipitation rate, displayed solutions characterized by increasing average biomass density (Fig. 2). The biomass density values for the amorphous patterns, averaged across the whole domain, were lower than those of the uniform solution at almost every point considered in the parameter space. However, as the precipitation rate decreased, close to the point at which the spatial model would tip into a bare soil state ($p = 0.993$), the patterned solution allowed the survival of small patches in which the biomass content decreased slowly. This resulted in an average biomass density value larger than the biomass density value of the uniform solution close to the tipping point (Fig. 2).

For further decreases in precipitation rate, patches were observed to survive even beyond the tipping point: a small stable patch could survive until p reached 0.5, even though the mathematical analysis showed that below that threshold, there is no stable solution, aside from the bare soil.

Rainfall also influences the shape of the amorphous patterns: increasing the precipitation rate shifts the patterns from spots to labyrinths and, ultimately, to labyrinthine gaps (Fig. 4). The cross sections of the biomass field (Fig. 4) revealed a square-wave front for all the cases. Appendix C shows that runs performed over longer times display a patch coarsening effect, similarly to Kletter et al. (2012): an integration performed over 460 time units at $p = 3$ displays how the irregular patterns are not stable (Fig. 5). Rather, the patches continued to evolve throughout the integration period by expanding and merging larger patches at the expense of the smaller ones, which died out (Fig. 5 and Appendix C). However, the average patch size ($\overline{R}(t)$) scaled with time following a power law of the form $\overline{R}(t) \simeq t^{1/2}$. This scaling behaviour enabled quantitative analyses once the patch growth rate had slowed, i.e., after a few tens of time units. An explanation of the mechanism underlying both square wave fronts and the patch coarsening effect is discussed in the next section.

4. Discussion

This work introduced a representation of the whole spectrum of plant clonal growth strategies within a classical model of pattern formation in drylands (Gilad et al., 2004), thereby representing the guerrilla strategy in dryland models for the first time. The clonal growth model

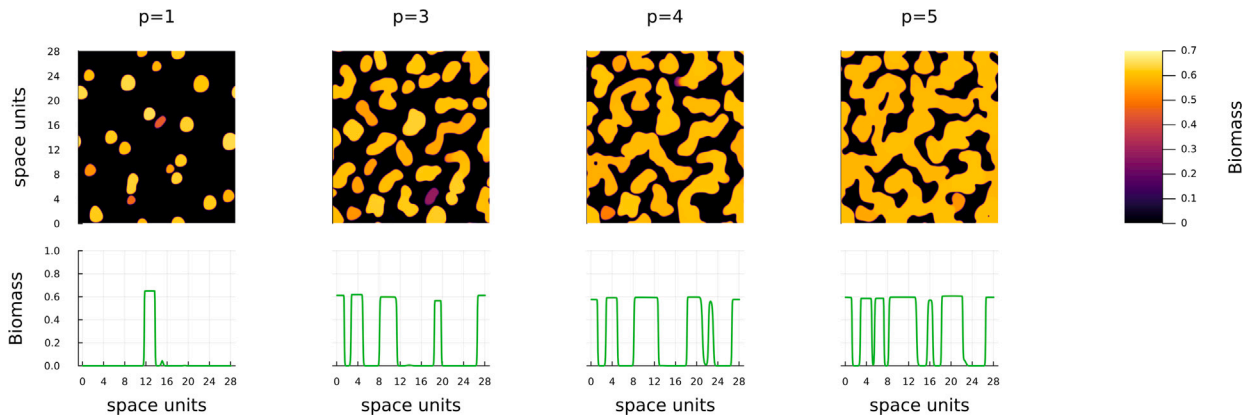

Fig. 4. Four different levels of precipitation p (left to right) (Top) Maps of plant biomass density at 100 time steps. Vegetation self-organizes into amorphous patterns of different shapes: with increasing precipitation, we observe spots, labyrinths, and labyrinthine gaps. The biomass fields were initialized with identical random biomass density initial conditions. (Bottom) Cross-section of the above biomass field taken horizontally in the middle of the plot, showing square-wave fronts.

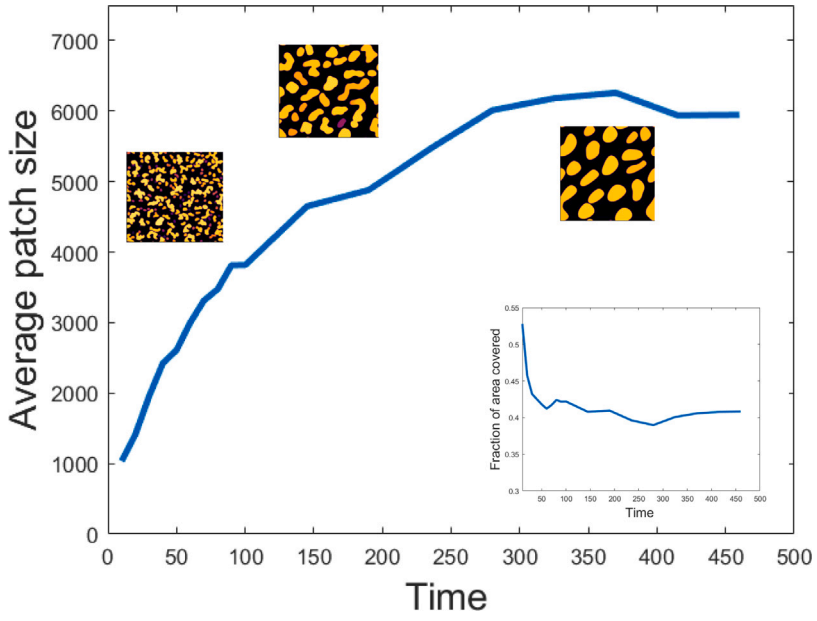

Fig. 5. Temporal series of the average patch size and fraction of area covered by vegetation (inset), measured in pixels. The images show the evolution of a biomass field, initialized randomly, at times $t = 20$, 190, 370, with an intermediate precipitation level ($p = 3$)

produced spatially amorphous vegetation patterns when precipitation decreased below values that ensured the stability of the uniform state under heterogeneous perturbations. These patterned states survived even below the tipping point of the homogeneous system, showing that, in this framework, self-organization allows for the avoidance of abrupt transitions between the two homogeneous states when the control parameter decreases below the critical point (Rietkerk et al., 2021). The amorphous patterns were gaps, labyrinths or spots with decreasing precipitation rate, and they coarsened over time.

The observed amorphous patterns differ from Turing patterns as the patches are not geometrically regular, they lack periodicity and they display rather squared-wave fronts, instead of the smooth, sinusoidal profiles predicted by Turing's linear framework (e.g., those seen in Fig. E.11b). This suggests that the underlying mechanism of pattern formation differs from the well-known scale-dependent feedback (e.g. Rietkerk et al., 2002), that typically leads to Turing patterns. Instead, our clonal growth model outputs are closer to those described in Siteur et al. (2023), where solutions of the nonlinear system emerge through a "density-dependent feedback", allowing larger patches to absorb more resources at the expense of neighbouring smaller ones. This class of solutions is referred to as "far-from-equilibrium patterns" (Veerman et al., 2021). Such density-dependent feedback can establish an asymmetric competition for resources that may lead to the formation of irregular patterns, similar to what is observed in phase separation processes (Siteur et al., 2023).

The squared-wave fronts observed with this model indicate strong spatial scale separation, which aligns more closely with density-dependent feedback and far-from-equilibrium mechanisms than with classical Turing patterns (Veerman et al., 2021).

We thus hypothesize that the amorphous patterns observed with our numerical simulations belong to the far-from-equilibrium class of patterns, also because the simulations suggest that finite-amplitude perturbations are required to generate patterns (Appendix D), even in cases where the uniform state is theoretically (i.e., according to Turing analysis) unstable. This behaviour reflects a departure from classical Turing instabilities, where infinitesimal perturbations are sufficient to destabilize the uniform state and initiate pattern formation. Instead, far-from-equilibrium patterns do not emerge directly from a linear instability of the homogeneous state, but instead require finite-amplitude perturbations to break the stability of the homogeneous state, even

when linear stability analysis suggests instability. This reflects a form of bistability, where the system retains the capacity to revert to the homogeneous state unless a sufficiently strong "nudge" pushes it into a patterned configuration. Thus, far-from-equilibrium patterns should be interpreted as solutions of the full nonlinear system; their existence and persistence therefore cannot be inferred from linear stability or Turing analyses alone, but arise from the interplay of the strong non-linearity of the guerrilla expansion term (see Fig. 1 in Veerman et al., 2021).

Our amorphous patterns share some similarities with irregular, scale free patterns, such as the lack of single-mode periodicity and the non-geometrical patch shapes. For example, the inclusion of seed dispersal with an integral global term in Pueyo et al. (2010) and Baudena and Rietkerk (2013) leads to patterns that are less regular than those of simpler models such as Rietkerk et al. (2002) and Gilad et al. (2004). In another model similar to ours (but including diffusion for plant lateral growth), irregular patterns also form when a global term is included to represent global competition for water (von Hardenberg et al., 2010). This represents conditions in which surface water runoff is much faster than infiltration, or in which soil water diffusion is much quicker than water uptake by biomass. However, global resource competition (which, in our model, could represent soil water diffusion being much faster than water uptake by biomass, as, for simplicity, we did not represent infiltration dependence on biomass density) is not responsible for the amorphous pattern formation in our model. We showed this by reducing the water diffusion coefficient by a factor 50. Under this condition, the formation of regular patterns in the clonal growth model was not observed; the patches remained irregular with a generally rounder shape of the patches and in a lower number (Fig. 6). This was also shown by the transition from amorphous to regular patterns, obtained when the phalanx strategy prevailed with respect to the guerilla strategy (Appendix E). Thus, the mechanism underlying the formation of amorphous patterns in the clonal growth model is closely linked to the clonal expansion term rather than to global competition for resources.

The density-dependent feedback led to an increase in the average patch size over time (see Appendix C), a phenomenon known in literature as "patch coarsening effect" (Kletter et al., 2012; Meron, 2015). Similarly to the earlier results by Kletter et al. (2012) (which employed the same model and parameters from Gilad et al., 2007), the patch size distribution grows at a rate of $\simeq t^{1/2}C$, suggesting that an Ostwald-ripening phenomenon (i.e. the small patches merging in a single, large patch over time Voorhees, 1992) may exist also for the clonal growth model. This latter consideration implies that the system might continue to change for longer periods ($\simeq 10^6$ time units), culminating in the formation of a single, stable patch. However, we did not test this hypothesis due to the elevated computational cost associated with the guerrilla expansion term. We want to emphasize that, to observe coarsening, the model had to run over very long timescales (during which environmental conditions were constant), which are probably not relevant in ecological terms. The absence of periodic environmental disturbances, such as daily or seasonal forcing cycles, and of sparse and/or spatially heterogeneous perturbations, such as drought events or animal grazing, also limits the discussion of the realistic correspondence between coarsening and its ecological relevance.

Since our model did not include resource transport within the genet and assumed spatially homogeneous resources, plasticity was not represented explicitly as in Oborny et al. (2001); instead, our framework isolated the effects of a fixed "guerrilla-like" expansion term at a large environmental scale. In doing so, we extended the conceptual insights of Oborny et al. (2001) from the module scale to the scale of dryland vegetation patterning, showing that the predominance of a guerrilla strategy can generate spatial structures that are not captured in models focused on a single genet level. Similarly, we complemented the work of Herben and Wildová (2012) by spatially extending the investigation framework to investigate the emergence of amorphous patterns and the implications for the genet resilience under environmental stress. Further, Bennett et al. (2022) successfully reproduced the formation of secondary patches outside the original clusters thanks to a non-local (i.e. integral) expansion term, as expected under the guerrilla strategy This represents an advantage compared to our model; however, this work did not explicitly assesses whether the resulting structures qualify as Turing patterns (although the absence of square-wave fronts suggests that they are not far-from-equilibrium states either). Our work, instead, focused on a nonlinear local expansion mechanism that shows how the regularity associated with reaction–diffusion systems can be broken, leading to a different class of solutions.

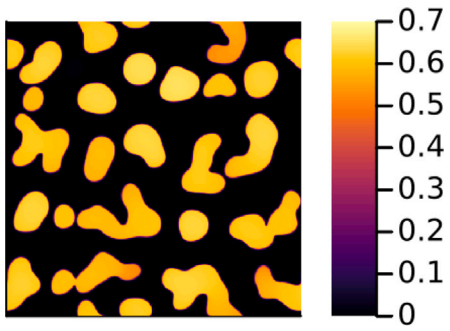

Fig. 6. Plant biomass density (colourmap) in space when soil water diffusion is largely reduced. The simulation was initialized with the same initial condition as in Fig. 4, but with the soil water diffusion reduced by a factor 50 with respect to the value in Table 1, for 100 time-steps. Reduced competition for water results in fewer patches. Still, it does not produce regular patterns, indicating that their irregular shape is not due to global competition for resources (von Hardenberg et al., 2010) but rather to the guerrilla expansion term.

Clonal growth is a widespread alternative to sexual reproduction in drylands; however, it is only partially represented in current dryland vegetation models. This work showed that incorporating the whole spectrum of clonal growth strategies can yield results that differ significantly from those of standard reaction–diffusion models, revealing a much richer diversity of pattern formation, ranging from regular, Turing-like structures associated with a predominant phalanx strategy to amorphous patterns related to a dominant guerrilla approach. Our model outputs (similarly to the empirical characterization of Reijers et al., 2021) show how clonal growth can generate spatial complexity independently of external heterogeneity. This highlights a previously underexplored route to amorphous spatial patterning, complementing existing mechanistic explanations such as non-local dispersal or scale-dependent feedbacks. The emergence of these patterns revealed the importance of extending the theoretical framework beyond Turing (i.e., linear) analyses. Finally, since pattern formation determines ecosystem existence and stability, our work suggests the necessity to include the whole spectrum of clonal growth strategies, possibly, in future works, by incorporating environmentally driven shifts between phalanx and guerrilla strategies when trying to predict dryland resilience to ongoing global change and potentially suggesting new conservation and restoration measures in these environments.

CRediT authorship contribution statement

Andrea Davin: Writing – original draft, Visualization, Software, Methodology, Investigation, Formal analysis, Data curation, Conceptualization. **Jost von Hardenberg:** Writing – review & editing, Supervision, Software, Resources, Methodology, Conceptualization. **Paul M.J. Berghuis:** Writing – review & editing, Supervision, Conceptualization. **Ángeles G. Mayor:** Writing – review & editing, Resources, Funding acquisition, Conceptualization. **Enrico Magazzino:** Writing – review & editing, Investigation. **Max Rietkerk:** Writing – review

& editing, Supervision, Methodology, Conceptualization. **Frits Veerman:** Methodology, Investigation. **Mara Baudena:** Writing – review & editing, Supervision, Methodology, Investigation, Conceptualization.

Declaration of competing interest

The authors declare that they have no known competing financial interests or personal relationships that could have appeared to influence the work reported in this paper.

Acknowledgements

This publication is part of the project with file number OCENW.XS21.4.031 of the research programme Open Competition XS funded by the Dutch Research Council (NWO).

The research of MR is supported by the European Research Council (ERC-Synergy project RESILIENCE, proposal nr. 101071417) and by the Dutch Research Council (NWO 'Resilience in complex systems through adaptive spatial pattern formation', project nr. OCENW.M20.169). This work was conducted as part of the EMBRACER program, the Earth System Feedback Research Centre, and was financially supported by the SUMMIT program of the Dutch Research Council (NWO).

M.B. acknowledges the Italian National Biodiversity Future Center (NBFC): National Recovery and Resilience Plan (NRRP), Mission 4 Component 2 Investment 1.4 of the Italian Ministry of University and Research; funded by the European Union—NextGenerationEU (Project code CN00000033). A.G.M. acknowledges funding from grant PID2023-148484OB-I00 funded by MICIU/AEI/10.13039/501100011033/ FEDER, EU.

Appendix A. Calculations

A.1. Solutions of the kernel term integrals

Following e.g. Gilad et al. (2007), we report here the complete calculations of the kernel term integrals g_b and g_w from Eq. (2), necessary for the linear stability analysis in case of a spatially-dependent perturbation of the b and w fields. The first step consists expanding the g term, obtaining

$$g(\mathbf{x},\mathbf{x}') = g_0(\mathbf{x},\mathbf{x}') + g_1(\mathbf{x},\mathbf{x}')\delta b(\mathbf{x})$$

where

$$g_0(\mathbf{x},\mathbf{x}') = g(\mathbf{x},\mathbf{x}')|_{b_0} = \frac{1}{2\pi} e^{-|\mathbf{x}-\mathbf{x}'|^2/2\sigma^2}$$

$$g_1(\mathbf{x},\mathbf{x}') = \frac{\partial}{\partial b}[g(\mathbf{x},\mathbf{x}')]|_{b_0}$$

in which $\sigma = 1 + \eta b_0$ and $|\mathbf{x}-\mathbf{x}'|^2 = (x-x')^2 + (y-y')^2$.

The first kernel term analysed is the root-augmentation feedback g_b.

After the introduction of spatially-dependent, periodic perturbations of the two variables characterized by a constant wavelength k: $\delta b(x,t) = a_b \exp(ik\cdot x + \lambda t)$ and $\delta w(x,t) = a_w \exp(ik\cdot x + \lambda t)$, the term becomes:

$$\begin{aligned} g_b &= \nu[\int_\Omega g(\mathbf{x},\mathbf{x}')(w_0 + \delta w(\mathbf{x}'))\, d\mathbf{x}' \\ &\quad + \int_\Omega \frac{w_0\eta}{\sigma^3}|\mathbf{x}-\mathbf{x}'|^2 g(\mathbf{x},\mathbf{x}')\delta b(\mathbf{x})\, d\mathbf{x}'\cdot] \end{aligned}$$

where $\mathbf{x} = \begin{pmatrix} x \\ y \end{pmatrix}$ and $g(\mathbf{x},\mathbf{x}') = \frac{1}{2\pi}\exp(-\frac{|\mathbf{x}-\mathbf{x}'|^2}{2\sigma^2})$.

Assuming an infinite domain, the first integral can be rewritten as a Gaussian integral plus another slightly more complicated one. In contrast, the second integral is simply the integral of a derivative. Remembering that the integrals are solved with respect to a 2-D variable and expanding the perturbation, the kernel term becomes:

$$\begin{aligned} g_b &= \nu[w_0\sigma^2 + 2\eta\sigma w_0 \delta b(\mathbf{x}) + \frac{1}{2\pi}\int_\Omega e^{-\frac{|\mathbf{x}-\mathbf{x}'|^2}{2\sigma^2}} a_w e^{ik\mathbf{x}'}\, d\mathbf{x}'] \\ &= \nu[w_0\sigma^2 + 2\eta\sigma w_0\delta b(\mathbf{x}) + \frac{1}{2\pi}\int_\Omega e^{-\frac{|\mathbf{z}|^2}{2\sigma^2}} a_w e^{ik(\mathbf{z}+\mathbf{x})}\, d\mathbf{z}] \\ &= \nu[w_0\sigma^2 + 2\eta\sigma w_0\delta b(\mathbf{x}) + \sigma^2 e^{-\frac{k^2\sigma^2}{2}}\delta w(\mathbf{x})] \end{aligned}$$

where the integration variable was substituted to $\mathbf{z} = \mathbf{x}' - \mathbf{x}$ in order to simplify the calculation.

The solution for the term g_w differs from the one presented above:

$$\begin{aligned} g_w =& \gamma[\int_\Omega g(\mathbf{x}',\mathbf{x})(b_0 + \delta b(\mathbf{x}'))\, d\mathbf{x}' + \\ & \int_\Omega \frac{b_0\eta}{\sigma^3}|\mathbf{x}'-\mathbf{x}|^2 g(\mathbf{x}',\mathbf{x})\delta b(\mathbf{x}')\, d\mathbf{x}'] \end{aligned} \tag{A.1}$$

While the first integral can be solved as in the previous case, the second needs more complicated calculations, since the perturbative term depends on the integral variable:

$$\begin{aligned} g_w &= \gamma[b_0\sigma^2 + \sigma^2 e^{-\frac{k^2\sigma^2}{2}}\delta b(\mathbf{x}) + \frac{1}{2\pi}\int_\Omega e^{-\frac{|\mathbf{z}|^2}{2\sigma^2}} a_b e^{ik(\mathbf{z}+\mathbf{x})}\, d\mathbf{z}] \\ &= \gamma[w_0\sigma^2 + +\sigma^2 e^{-\frac{k^2\sigma^2}{2}}\delta b(\mathbf{x}) + \frac{b_0\eta}{2\pi\sigma^3}\delta b(\mathbf{x})\int_\Omega |\mathbf{z}|^2 e^{-\frac{|\mathbf{z}|^2}{2\sigma^2}} e^{ik(\mathbf{z})}\, d\mathbf{z}] \end{aligned}$$

Focusing on the last term, we obtain, after defining $C(t) = \frac{b_0\eta}{2\pi\sigma^3}\delta b(\mathbf{x})$ for the sake of simplicity.

$$\begin{aligned} C(t)\int_\Omega |\mathbf{z}|^2 e^{-\frac{|\mathbf{z}|^2}{2\sigma^2}} e^{ik(\mathbf{z})}\, dz &= C(t)[\int_\Omega |\mathbf{z}|^2 e^{-\frac{|\mathbf{z}|^2}{2\sigma^2}+ik\mathbf{z}}\, d\mathbf{z}] \\ &= C(t)[\int_\Omega |\mathbf{z}|^2 e^{-\frac{1}{2\sigma^2}(\mathbf{z}-i\sigma^2 k)^2 - \frac{\sigma^2k^2}{2}}\, d\mathbf{z}] \\ &= C(t)e^{-\frac{\sigma^2k^2}{2}}[\int_\Omega (\mathbf{z}' + i\sigma^2 k)^2 e^{-\frac{\mathbf{z}'^2}{2\sigma^2}}\, d\mathbf{z}'] \\ &= C(t)e^{-\frac{\sigma^2k^2}{2}} \\ &\quad \times[\int_\Omega (\mathbf{z}'2 + 2i\sigma^2 k\mathbf{z}' - \sigma^4k^2)e^{-\frac{\mathbf{z}'^2}{2\sigma^2}}\, d\mathbf{z}'] \end{aligned}$$

The new variable $\mathbf{z}'$ keeps the integration over an infinite domain. The latter integral can be divided into three parts, each of which is solved using integration by parts, and remembering that the integral variable is in 2-D:

$$\begin{aligned} & C(t)e^{-\frac{\sigma^2k^2}{2}}[\int_\Omega \mathbf{z}'2e^{-\frac{\mathbf{z}'^2}{2\sigma^2}}\, d\mathbf{z}'] \\ &= C(t)e^{-\frac{\sigma^2k^2}{2}}[\int_\Omega -\mathbf{z}'\sigma^2(-\frac{\mathbf{z}'}{\sigma^2}e^{-\frac{\mathbf{z}'^2}{2\sigma^2}})\, d\mathbf{z}'] \end{aligned}$$

$$= 2\sigma^4\pi C(t)e^{-\frac{\sigma^2k^2}{2}} \tag{A.2}$$

$$C(t)e^{-\frac{\sigma^2k^2}{2}}[\int_\Omega 2i\sigma^2k\mathbf{z}'e^{-\frac{\mathbf{z}'^2}{2\sigma^2}}\, d\mathbf{z}'] = 0 \tag{A.3}$$

$$C(t)e^{-\frac{\sigma^2k^2}{2}}[\int_\Omega -\sigma^4k^2e^{-\frac{\mathbf{z}'^2}{2\sigma^2}}\, d\mathbf{z}'] = -2\pi\sigma^6k^2 \tag{A.4}$$

Adding all the terms, it is obtained that:

$$\begin{aligned} g_w &= \gamma[b_0\sigma^2 + \sigma e^{-\frac{\sigma^2k^2}{2}}\delta b(\mathbf{x})(\sigma + \eta b_0(1-\sigma^2k^2))] \\ &= \gamma[b_0\sigma^2 + \sigma e^{-\frac{\sigma^2k^2}{2}}\delta b(\mathbf{x})(1 + \eta b_0(2-\sigma^2k^2))] \end{aligned}$$

In the case of uniform perturbations, $g(x,x')$ reduces to $g(x') = \frac{1}{2\pi}\exp(-\mathbf{x}'^2/2\sigma^2)$ and the solutions can be obtained as simple Gaussian integrals, leading to $g_w = \gamma b_0\sigma^2$ and $g_b = \nu w_0\sigma^2$.

A.2. Guerrilla expansion term expansion in 2-D

$$\begin{aligned} \nabla\cdot(bw\frac{\nabla b}{|\nabla b|}) &= \partial_x(bw\frac{\partial_x b}{|\nabla b|}) + \partial_y(bw\frac{\partial_y b}{|\nabla b|}) \\ &= \frac{(\partial_x(bw\partial_x b))|\nabla b| - (bw\partial_x b)\partial_x|\nabla b|}{|\nabla b|^2} + y\leftrightarrow x \\ &= \frac{1}{|\nabla b|^2}[((\partial_x b)^2 w + b\partial_x w\partial_x b + bw\partial_{xx}b)|\nabla b| \end{aligned}$$

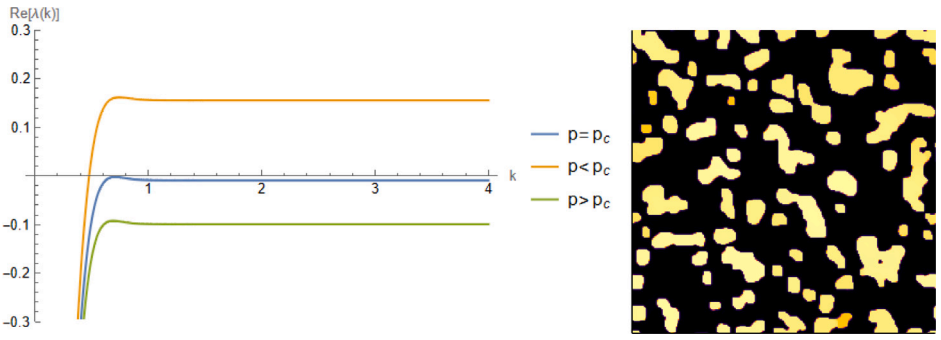

Fig. B.7. Real part of the largest eigenvalue of the homogeneously vegetated state, plotted as a function of the wavelength number k for three different values of p (left). Consequences on the numerical solution of the biomass density equation (right).

$$
\begin{aligned}
&-\frac{1}{2}\frac{bw\partial_x b}{|\nabla b|}((2\partial_x b)\partial_{xx}b + (2\partial_y b)\partial_{xy}b)] + y \leftrightarrow x \\
&= \frac{1}{|\nabla b|}[w(\partial_x b)^2 + (\partial_y b)^2 + b(\partial_{xx}b + \partial_{yy}b)] \\
&\quad + \frac{1}{|\nabla b|}[b(\partial_x w\partial_x b + \partial_y w\partial_y b)] \\
&\quad - \frac{1}{|\nabla b|^3}bw[(\partial_x b)^2\partial_{xx}b + (\partial_y b)^2\partial_{yy}b + 2(\partial_x b)(\partial_y b)(\partial_{xy}b)] \\
&= w|\nabla b| + \frac{bw}{|\nabla b|}\nabla^2 b + \nabla w \cdot \frac{b\nabla b}{|\nabla b|} \\
&\quad - \frac{bw}{|\nabla b|^3}((\partial_x b)^2\partial_{xx}b + (\partial_y b)^2\partial_{yy}b + 2(\partial_x b)(\partial_y b)(\partial_{xy}b))
\end{aligned}
$$

A.3. First-order periodic perturbation of the guerrilla expansion term

The two variables are now defined as composed of a homogeneous part, plus a periodic perturbation of wavelength k:

$b_0 + \delta b(\mathbf{x}) = b_0 + a\exp(i\mathbf{k}\cdot\mathbf{x})$ and

$w_0 + \delta w(\mathbf{x}) = w_0 + a\exp(i\mathbf{k}\cdot\mathbf{x})$

in which $\mathbf{x} = \begin{pmatrix} x \\ y \end{pmatrix}$ and $\mathbf{k} = \begin{pmatrix} k_x \\ k_y \end{pmatrix}$

If these terms are substituted in the clonal growth function, it is obtained that:

$$
\begin{aligned}
&(w_0 + \delta w(\mathbf{x}))|\nabla\delta b(\mathbf{x})| + \frac{(b_0 + \delta b(\mathbf{x}))(w_0 + \delta w(x))}{|\nabla\delta b(\mathbf{x})|}\nabla^2(\delta b(\mathbf{x})) \\
&-\frac{(b_0 + \delta b(\mathbf{x}))(w_0 + \delta w(\mathbf{x}))}{|\nabla\delta b(\mathbf{x})|^3}((\partial_x\delta b(\mathbf{x}))^2\partial_{xx}\delta b(\mathbf{x}) \\
&+ (\partial_y\delta b(\mathbf{x}))^2\partial_{yy}\delta b(\mathbf{x}) + 2\partial_x\delta b(\mathbf{x})\partial_y\delta b(\mathbf{x})\partial_{xy}\delta b(\mathbf{x})) \\
&+ \nabla(w_0 + \delta w(\mathbf{x}))\cdot\frac{(b_0 + \delta b(\mathbf{x}))\nabla(\delta b(\mathbf{x}))}{|\nabla\delta b(\mathbf{x})|}
\end{aligned}
$$

Each term is separated to facilitate reading. Only first-order terms are kept:

$$
\begin{aligned}
(w_0 + \delta w(\mathbf{x}))|\nabla\delta b(\mathbf{x})| &= (w_0 + \delta w(\mathbf{x}))\sqrt{(\partial_x\delta b(\mathbf{x}))^2 + (\partial_y\delta b(\mathbf{x}))^2} \\
&= (w_0 + \delta w(\mathbf{x}))\sqrt{(ik_x\delta b(\mathbf{x}))^2 + (ik_y\delta b(\mathbf{x}))^2} \\
&= (w_0 + \delta w(\mathbf{x}))\sqrt{-(k_x^2 + k_y^2)\delta b^2(\mathbf{x})} \\
&= w_0 i|\mathbf{k}|\delta b(\mathbf{x}) \qquad \text{(A.5)}
\end{aligned}
$$

$$
\begin{aligned}
&\frac{(b_0 + \delta b(\mathbf{x}))(w_0 + \delta w(\mathbf{x}))}{|\nabla\delta b(\mathbf{x})|}\nabla^2(\delta b(\mathbf{x})) \\
&= (b_0 + \delta b(\mathbf{x}))(w_0 + \delta w(\mathbf{x}))(-\frac{|\mathbf{k}|^2\delta b(\mathbf{x})}{i|\mathbf{k}|\delta b(\mathbf{x})}) \\
&= ib_0w_0|\mathbf{k}| + iw_0|\mathbf{k}|\delta b(\mathbf{x}) + ib_0|\mathbf{k}|\delta w(\mathbf{x}) \qquad \text{(A.6)}
\end{aligned}
$$

$$
\begin{aligned}
&\frac{(b_0 + \delta b(\mathbf{x}))(w_0 + \delta w(\mathbf{x}))}{|\nabla\delta b(\mathbf{x})|^3}((\partial_x\delta b(\mathbf{x}))^2\partial_{xx}\delta b(\mathbf{x}) \\
&+ (\partial_y\delta b(\mathbf{x}))^2\partial_{yy}\delta b(\mathbf{x}) + 2\partial_x\delta b(\mathbf{x})\partial_y\delta b(\mathbf{x})\partial_{xy}\delta b(\mathbf{x})) \\
&= \frac{(b_0 + \delta b(\mathbf{x}))(w_0 + \delta w(\mathbf{x}))}{-i|\mathbf{k}|^3\delta b^3(\mathbf{x})}((\delta b^3(\mathbf{x}))(ik_x)^2(ik_x)^2 \\
&+ (\delta b^3(\mathbf{x}))(ik_y)^2(ik_y)^2 + 2((\delta b^3(\mathbf{x}))(ik_x)(ik_y)(-k_xk_y))) \\
&= \frac{(b_0 + \delta b(\mathbf{x}))(w_0 + \delta w(\mathbf{x}))}{-i|\mathbf{k}|^3}(k_x^4 + k_y^4 + 2(k_xk_y)^2) \\
&= ib_0w_0|\mathbf{k}| + iw_0\mathbf{k}\delta b(\mathbf{x}) + ib_0|\mathbf{k}|\delta w(\mathbf{x}) \qquad \text{(A.7)}
\end{aligned}
$$

$$
\begin{aligned}
&\delta w(\mathbf{x})\cdot\frac{(b_0 + \delta b(\mathbf{x}))\nabla(\delta b(\mathbf{x}))}{|\nabla\delta b(\mathbf{x})|} \\
&= \frac{b_0 + \delta b(\mathbf{x})}{i|\mathbf{k}|\delta b(\mathbf{x})}(\partial_x\delta b(\mathbf{x})(\partial_x\delta w(\mathbf{x})) + (\partial_y\delta b(\mathbf{x}))(\partial_y\delta w(\mathbf{x}))) \\
&= \frac{b_0 + \delta b(\mathbf{x})}{i|\mathbf{k}|\delta b(\mathbf{x})}((-k_x^2\delta b(\mathbf{x})\delta w(\mathbf{x})) + (-k_y^2\delta b(\mathbf{x})\delta w(\mathbf{x}))) \\
&= \frac{b_0 + \delta b(\mathbf{x})}{i|\mathbf{k}|\delta b(\mathbf{x})}(-|\mathbf{k}|^2\delta b(\mathbf{x})\delta w(\mathbf{x})) = i|\mathbf{k}|b_0\delta w(\mathbf{x}) \qquad \text{(A.8)}
\end{aligned}
$$

Summing (and subtracting) the four terms, it is obtained that:

$$
\begin{aligned}
&\text{(A.5)} + \text{(A.6)} - \text{(A.7)} + \text{(A.8)} \\
&= iw_0|\mathbf{k}|\delta b(\mathbf{x}) + ib_0w_0|\mathbf{k}| + iw_0|\mathbf{k}|\delta b(\mathbf{x}) + ib_0|\mathbf{k}|\delta w(\mathbf{x}) \\
&-(ib_0w_0|\mathbf{k}| + iw_0|\mathbf{k}|\delta b(\mathbf{x}) + ib_0|\mathbf{k}|\delta w(\mathbf{x})) + ib_0|\mathbf{k}|\delta w(\mathbf{x}) \\
&= i|\mathbf{k}|(w_0\delta b(\mathbf{x}) + b_0\delta w(\mathbf{x}))
\end{aligned}
$$

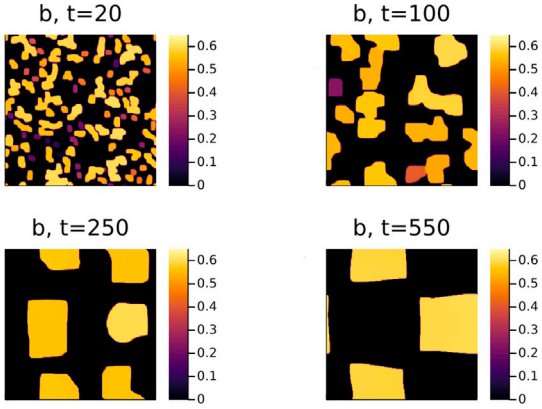

Fig. B.8. Evolution of a randomized biomass field of size 256 × 256 grid points for a non-regularized system. After ≃ 500 non-dimensional time units, the system reached stability.

Appendix B. Guerrilla expansion term's issues

In Section 2.1, it was explained how the Laplacian term in the biomass density equation serves as a regularizer for the system. Without

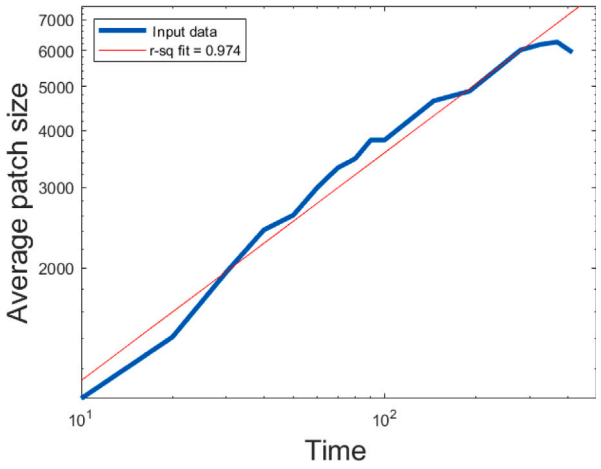

Fig. C.9. Average patch size for $p = 3$ as a function of time (in time steps) in a log–log plane. The R-squared value displays the degree of goodness of the fit with a function proportional to $t^{1/2}$.

this term, for a wide range of precipitation rates, the homogeneously vegetated state would be unstable to any periodic perturbation of wavelength $k > 0.6$, with the fastest-growing mode being near this threshold, followed by an infinite number of modes that grows with the same, slightly lower than that of the fastest-growing mode, velocity (Fig. B.7, left panel).

This peculiar form is due to the absence of a wavelength-selecting mechanism in the biomass density equation, which reflects on the eigenvalues functions: in fact, while in a diffusive system the Laplacian contributes with a factor $-k^2$ to the equation for the evolution of a perturbation (which usually gives a parabolic shape to the plot of the real part of the eigenvalues relative to the solution against k), in the clonal growth model, the guerrilla expansion term adds the two imaginary terms $ik(w_0\delta b(x,t) + b_0\delta w(x,t))$, reported in Section 3.1.

The absence of regularization leads to critical numerical issues: the possibility of the system amplifying perturbations with infinite wavenumbers necessitates infinite resolution in numerical solutions, which is an absurd requirement.

If not properly resolved, this issue leads to the formation of square patches (a sign that the numerical method is failing) and, after a few hundreds time-units of iteration, to the cessation of the system's evolution (Fig. B.8).

Appendix C. Coarsening

The patch coarsening effect has already been observed in Gilad's 2007 model, which resulted in an average patch size increasing with time at a rate of $t^{\frac{1}{2}}$, while maintaining the total area covered by the biomass unchanged after a few decades (Kletter et al., 2012).

Similarly, in the clonal growth model the fraction of area covered became rather stable after $\simeq$ 50 time units, with patches growing at a rate proportional to $t^{1/2}$ (Fig. C.9), opening up to the possibility that the system keep changing, until at long scale, only a single, round patch would remain, as observed in Kletter et al. (2012) (see Fig. C.9).

Appendix D. Periodic initial conditions

The clonal growth model produced regular patterns when initialized with periodic initial conditions with a large amplitude (see Section 2.3.3.) With such initial regular forcing, the model was able to amplify perturbations characterized by wavelengths that, according to the Turing stability analysis presented in Section 3.1.2, should have been eliminated by the system. Fig. D.10 shows how a perturbation characterized by $k \simeq 0.35$ is amplified by the system if its initial amplitude is large enough. Despite their regularity, the square-wave fronts and the necessity of a finite-amplitude perturbation question the identification of these patterns with Turing patterns, as, for them to arise, even an infinitesimal perturbation is sufficient to trigger pattern formation.

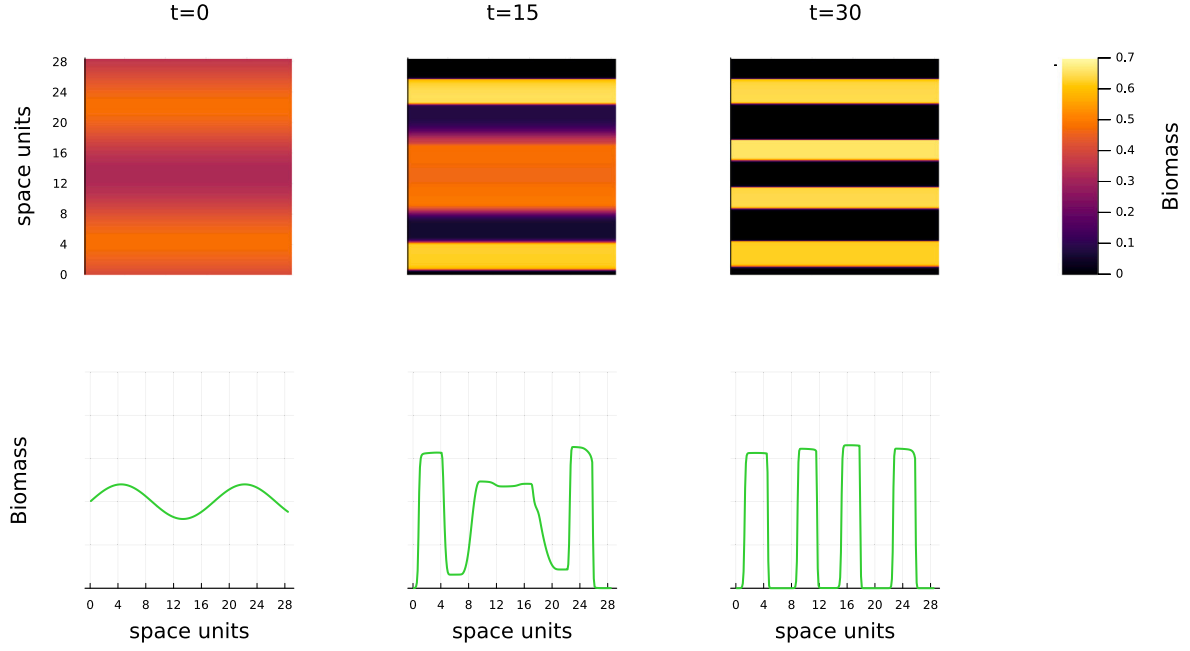

Fig. D.10. Time evolution of a biomass field perturbed with the "periodic initial conditions" described in Section 2.3.3. (Top) stripes arising from the perturbed homogeneous field. (Bottom) biomass field cross section showing the square wave fronts.

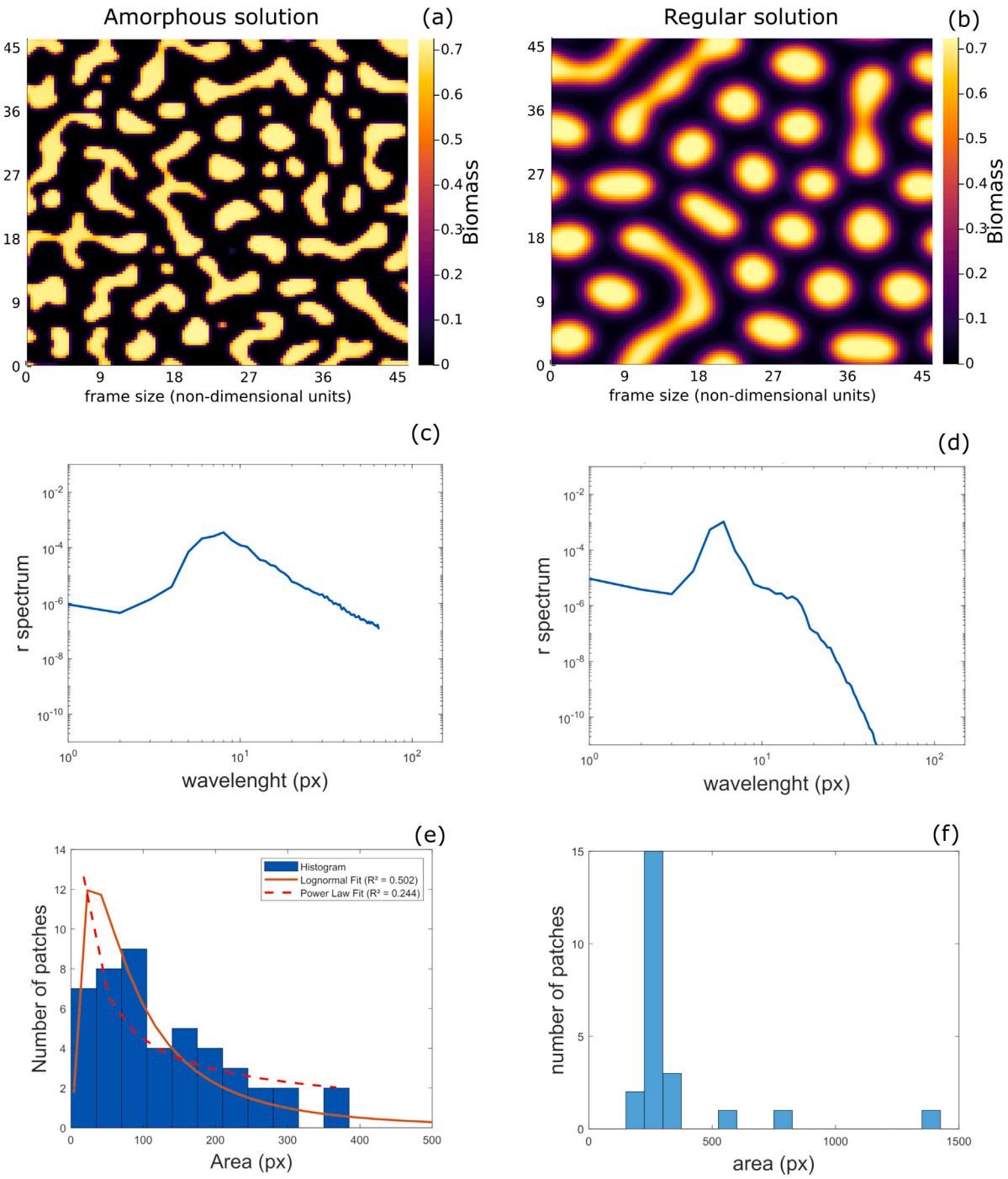

Fig. E.11. Comparison between the patterns obtained with dominant guerilla (left column) and phalanx (right column) strategies. (a, b) amorphous and periodic solutions for biomass density obtained by modifying the parameters c and δ_b. (c, d) their respective R-spectra, indicating that the amorphous solution lacks of a distinct autocorrelation length. (e, f) The patch size distributions, showing how broad it is in the amorphous case compared to the periodic one, which is constrained almost to a single bin. Results for the enlarged domain runs after 75 time units.

Appendix E. From amorphous to regular patterns

In this section, we discuss how the prevailing clonal growth strategy adopted by the vegetation affects pattern formation, i.e., whether the solution will be regular or amorphous. To this end, we present a spatial analysis of two biomass fields representing the two strategies, obtained by running the model for 75 time units on a domain enlarged to 46 length units, thus larger than the one used in Section 3.2. The two runs differ in the values of the clonal growth and biomass diffusion coefficients. With the first setting, we obtained amorphous patterns, with parameters representing plants with a dominant guerilla strategy (i.e., $c = 0.2$ and $\delta_b = 0.0005$, as in the other runs presented here Fig. E.11(a). With the second parameter setting, representing a predominantly phalanx growth strategy ($c = 0.05$ and $\delta_b = 0.333$, Fig. E.11b), we obtained a "periodic pattern". The value of the parameter δ_b was chosen equal to the value used in Gilad et al. (2007). In both runs the precipitation rate was $p = 4$.

To quantify the differences in the pattern geometry, the analysis focuses on the radial spectra by identifying a characteristic length scale of the pattern and on the patch size distribution. The presence

of a characteristic length scale would be an indicator of periodicity, while its absence, correlated with a broad, power law-like patch size distribution, identifies scale free patterns (von Hardenberg et al., 2010) As shown in Fig. E.11, the integration reveals that a predominantly guerrilla growth strategy leads to the formation of amorphous patterns. These solutions are characterized by the absence of a well-defined peak in the radial spectrum (Fig. E.11c), unlike in the periodic case (Fig. E.11d), and by a broader patch size distribution compared to that of the periodic pattern (Figs. E.11e, f). Although broader, the patch size distribution does not follow a power law-like distribution. Instead, a log-normal function better fits the patch size distribution (although the fit remains poor relative to our results). Therefore, the amorphous patterns produced by the model cannot be identified as irregular patterns as well (von Hardenberg et al., 2010). In summary, while a dominant phalanx strategy promotes the emergence of geometric patterns with well-defined periodicity and relatively uniform patch sizes, a predominantly guerrilla strategy drives the system away from this regularity, resulting in less ordered and more heterogeneous structures.

Appendix F. Homogeneous vegetated state

The non-trivial homogeneous steady state (b_0, w_0) solves the equations

$$-1 + (1 - b_0)g_w = 0, \quad p - \upsilon w_0 - g_w w_0 = 0, \tag{F.1}$$

cf. (1). Evaluating the expressions of g_b and g_w (2) for constant and homogeneous $b = b_0$ and $w = w_0$ yields

$$g_w = \gamma b_0 (1 + \eta b_0)^2, \quad g_b = \nu w_0 (1 + \eta b_0)^2. \tag{F.2}$$

Solving for w_0 in terms of b_0 and substitution of the result in the other equation yields

$$\upsilon + \gamma b_0 (1 + \eta b_0)^2 = \nu p (1 - b_0)(1 + b_0 \eta)^2, \tag{F.3}$$

to be solved for b_0. This is a cubic equation for b_0, whose explicit solutions can be expressed using Cardano's formula. Function analysis of the left- and right-hand side of Eq. (F.3) reveals that there exists a unique, real, positive solution $b_0 < 1$ to (F.3) if and only if $\left(\frac{1}{2} - \eta\right)(\nu p - \upsilon) > 0$.

Data availability

The Julia scripts used for this project are available at https://github.com/A-Davin/clonal_guerrilla.

References

Abatzoglou, J.T., Dobrowski, S.Z., Parks, S.A., Hegewisch, K.C., 2018. TerraClimate, a high-resolution global dataset of monthly climate and climatic water balance from 1958–2015. Sci. Data 5, 170191. http://dx.doi.org/10.1038/sdata.2017.191.

Bastiaansen, R., Jaïbi, O., Deblauwe, V., Eppinga, M.B., Siteur, K., Siero, E., Mermoz, S., Bouvet, A., Doelman, A., Rietkerk, M., 2018. Multistability of model and real dryland ecosystems through spatial self-organization. Proc. Natl. Acad. Sci. 115, 11256–11261. http://dx.doi.org/10.1073/pnas.1804771115.

Baudena, M., Rietkerk, M., 2013. Complexity and coexistence in a simple spatial model for arid savanna ecosystems. Theor. Ecol. 6, 131–141, URL: https://api.semanticscholar.org/CorpusID:16122403.

Bennett, J.J.R., Gomes, A.S., Ferré, M.A., Bera, B.K., Borghetti, F., Callaway, R.M., Meron, E., 2022. Evidence for scale-dependent root-augmentation feedback and its role in halting the spread of a pantropical shrub into an endemic sedge. PNAS Nexus 2, pgac294. http://dx.doi.org/10.1093/pnasnexus/pgac294, URL: https://doi.org/10.1093/pnasnexus/pgac294.

Borgogno, F., D'Odorico, P., Laio, F., Ridolfi, L., 2009. Mathematical models of vegetation pattern formation in ecohydrology. Rev. Geophys. 47, http://dx.doi.org/10.1029/2007RG000256.

Chen, X.-S., Xie, Y.-H., Deng, Z.-M., Li, F., Hou, Z.-Y., 2011. A change from phalanx to guerrilla growth form is an effective strategy to acclimate to sedimentation in a wetland sedge species carex brevicuspis (cyperaceae). Flora - Morphol. Distrib. Funct. Ecol. Plants 206, 347–350. http://dx.doi.org/10.1016/j.flora.2010.07.006.

Deblauwe, V., Barbier, N., Couteron, P., Lejeune, O., Bogaert, J., 2008. The global biogeography of semi-arid periodic vegetation patterns. Glob. Ecol. Biogeogr. 17, 715–723. http://dx.doi.org/10.1111/j.1466-8238.2008.00413.x.

Food and Agriculture Organization of the United Nations (FAO), 2004. Carbon sequestration in dryland soils. URL: https://www.fao.org/3/y5738e/y5738e00.htm.

Food and Agriculture Organization of the United Nations (FAO), 2019. Trees, forests and land use in drylands: The first global assessment. URL: www.fao.org/.

Gilad, E., von Hardenberg, J., Provenzale, A., Shachak, M., Meron, E., 2004. Ecosystem engineers: From pattern formation to habitat creation. Phys. Rev. Lett. 93, http://dx.doi.org/10.1103/PhysRevLett.93.098105.

Gilad, E., von Hardenberg, J., Provenzale, A., Shachak, M., Meron, E., 2007. A mathematical model of plants as ecosystem engineers. J. Theoret. Biol. 244, 680–691. http://dx.doi.org/10.1016/j.jtbi.2006.08.006.

von Hardenberg, J., Kletter, A.Y., Yizhaq, H., Nathan, J., Meron, E., 2010. Periodic versus scale-free patterns in dryland vegetation. Proc. R. Soc. B: Biol. Sci. 277, 1771–1776. http://dx.doi.org/10.1098/rspb.2009.2208.

von Hardenberg, J., Meron, E., Shachak, M., Zarmi, Y., 2001. Diversity of vegetation patterns and desertification. Phys. Rev. Lett. 87, 198101–1–198101–4. http://dx.doi.org/10.1103/PhysRevLett.87.198101.

Herben, T., Wildová, R., 2012. Community-level effects of plant traits in a grassland community examined by multispecies model of clonal plant growth. Ecol. Model. 234, 60–69.

Jenik, J., 1994. Clonal growth in woody plants: A review. Folia Geobot. Phytotaxon. 29, 291–306, URL: http://www.jstor.org/stable/4181274.

Kéfi, S., Génin, A., Garcia-Mayor, A., Guirado, E., Cabral, J.S., Berdugo, M., Guerber, J., Solé, R., Maestre, F.T., 2024. Self-organization as a mechanism of resilience in dryland ecosystems. Proc. Natl. Acad. Sci. 121, http://dx.doi.org/10.1073/pnas.2305153121.

Kéfi, S., Rietkerk, M., Alados, C.L., Pueyo, Y., Papanastasis, V.P., ElAich, A., De Ruiter, P.C., 2007. Spatial vegetation patterns and imminent desertification in Mediterranean arid ecosystems. Nature 449, 213–217.

Kletter, A.Y., von Hardenberg, J., Meron, E., 2012. Ostwald ripening in dryland vegetation. Commun. Pure Appl. Anal. 11, 261–273. http://dx.doi.org/10.3934/cpaa.2012.11.261.

Liu, F., Liu, J., Dong, M., 2016. Ecological consequences of clonal integration in plants. Front. Plant Sci. 7, 770.

Luo, W., Zhao, W., Zhuang, Y., 2018. Sand-burial and wind erosion promote oriented-growth and patchy distribution of a clonal shrub in dune ecosystems. Catena 167, 212–220.

Ma, Q., Qian, J., Tian, L., Liu, Z., 2019. Responses of belowground bud bank to disturbance and stress in the sand dune ecosystem. Ecol. Indic. 106, 105521.

Meron, E., 2015. Nonlinear Physics of Ecosystems. CRC Press, Taylor & Francis Group Boca Raton, FL, USA.

Oborny, B., 2019. The plant body as a network of semi-autonomous agents: A review. Philos. Trans. R. Soc. B 374, 20180371.

Oborny, B., Czárán, T., Kun, Á., 2001. Exploration and exploitation of resource patches by clonal growth: A spatial model on the effect of transport between modules. Ecol. Model. 141, 151–169.

Oborny, B., Mony, C., Herben, T., 2012. From virtual plants to real communities: A review of modelling clonal growth. Ecol. Model. 234, 3–19. http://dx.doi.org/10.1016/j.ecolmodel.2012.03.010.

Pessarakli, M., 2017. Growth responses of sacaton grass (sporobolus airoides torr.) and seashore paspalum (paspalum vaginatum swartz) under prolonged drought stress condition. Adv. Plants Agric. Res. 7, http://dx.doi.org/10.15406/apar.2017.07.00261.

Pueyo, Y., Kéfi, S., Díaz-Sierra, R., Alados, C.L., Rietkerk, M., 2010. The role of reproductive plant traits and biotic interactions in the dynamics of semi-arid plant communities. Theor. Popul. Biol. 78, 289–297. http://dx.doi.org/10.1016/j.tpb.2010.09.001.

Reijers, V.C., Hoeks, S., van Belzen, J., Siteur, K., de Rond, A.J.A., van de Ven, C.N., Lammers, C., van de Koppel, J., van der Heide, T., 2021. Sediment availability provokes a shift from Brownian to Lévy-like clonal expansion in a dune building grass. Ecol. Lett. 24, 258–268. http://dx.doi.org/10.1111/ele.13638.

Rietkerk, M., Bastiaansen, R., Banerjee, S., van de Koppel, J., Baudena, M., Doelman, A., 2021. Evasion of tipping in complex systems through spatial pattern formation. Science 374, http://dx.doi.org/10.1126/science.abj0359.

Rietkerk, M., Boerlijst, M.C., Van Langevelde, F., HilleRisLambers, R., de Koppel, J.v., Kumar, L., Prins, H.H.T., de Roos, A.M., 2002. Self-organization of vegetation in arid ecosystems. Amer. Nat. 160, 524–530.

Siero, E., Siteur, K., Doelman, A., Koppel, J.v.d., Rietkerk, M., Eppinga, M.B., 2019. Grazing away the resilience of patterned ecosystems. Amer. Nat. 193, 472–480. http://dx.doi.org/10.1086/701669.

Sintes, T., Marbà, N., Duarte, C.M., 2006. Modeling nonlinear seagrass clonal growth: Assessing the efficiency of space occupation across the seagrass flora. Estuaries Coasts 29, 72–80.

Siteur, K., Liu, Q.-X., Rottschäfer, V., van der Heide, T., Rietkerk, M., Doelman, A., Boström, C., van de Koppel, J., 2023. Phase-separation physics underlies new theory for the resilience of patchy ecosystems. Proc. Natl. Acad. Sci. 120, e2202683120.

Tsakalos, J., Ottaviani, G., Chelli, S., Rea, A., Elder, S., Dobrowolski, M., Mucina, L., 2022. Plant clonality in a soil-impoverished open ecosystem: Insights from south-west Australian shrublands. Ann. Botany 130, 981–990. http://dx.doi.org/10.1093/aob/mcac131.

Veerman, F., Mercker, M., Marciniak-Czochra, A., 2021. Beyond turing: Far-from-equilibrium patterns and mechano-chemical feedback. Philos. Trans. R. Soc. A: Math. Phys. Eng. Sci. 379, 20200278. http://dx.doi.org/10.1098/rsta.2020.0278, URL: https://royalsocietypublishing.org/doi/abs/10.1098/rsta.2020.0278. arXiv:https://royalsocietypublishing.org/doi/pdf/10.1098/rsta.2020.0278.

Voorhees, P.W., 1992. Ostwald ripening of two-phase mixtures. Annual Rev. Mater. Research 22, 197–215. http://dx.doi.org/10.1146/annurev.ms.22.080192.001213, URL: https://www.annualreviews.org/content/journals/10.1146/annurev.ms.22.080192.001213.

Winkler, E., Fischer, M., Schmid, B., 1999. Modelling the competitiveness of clonal plants by complementary analytical and simulation approaches. Oikos 85, 217–233, URL: http://www.jstor.org/stable/3546488.

Yu, F.-H., Wang, N., He, W.-M., Chu, Y., Dong, M., 2008. Adaptation of rhizome connections in drylands: Increasing tolerance of clones to wind erosion. Ann. Botany 102, 571–577. http://dx.doi.org/10.1093/aob/mcn119.